

Na₅FeS₄ as High-Capacity Positive Electrode Active Material for All-Solid-State Sodium Batteries

Yuta Doi, Tomoya Otono, Yushi Fujita, Raku Kato, Masato Torii, Jiong Ding, Shigeo Mori, Kota Motohashi, Atsushi Sakuda,* and Akitoshi Hayashi

Meeting the growing demand for energy storage systems requires the development of batteries that satisfy the requirements of high safety, low cost, and high energy density. All-solid-state sodium batteries with sulfide-based active materials are a promising energy storage technology because they satisfy these requirements. In particular, sodium-containing iron sulfides are attractive for positive electrode active materials because of their high capacities and ionic conductivities. In this study, Na₅FeS₄ is investigated as a positive electrode active material for all-solid-state sodium batteries. Na₅FeS₄ is synthesized by

ambient-pressure heat treatment using sodium polysulfides. All-solid-state cells using Na₅FeS₄ as a positive electrode active material exhibit a high reversible capacity of 480 mAh g⁻¹ at ≈25 °C. The active material mainly became amorphous during the initial charge, and this amorphous state contribute to reversible charge–discharge with high capacity. This study advances the development of low-cost and high-capacity sulfide positive electrode active materials for all-solid-state sodium batteries suitable for large-scale energy storage.

1. Introduction

The development of electric vehicles and smart electronic devices has led to increased demand for safe and inexpensive energy-storage devices with high energy density and long service life. While lithium-ion batteries (LIBs) are widely used for energy storage, their positive electrode active materials are expensive, necessitating the development of less expensive materials to enable large-scale energy storage. Compared to LIBs, sodium batteries are less expensive because sodium is one of the most abundant elements on earth, and all-solid-state sodium batteries, in which liquid electrolytes are replaced with inorganic solid electrolytes, are a particularly attractive technology owing to their high safety and high energy density.^[1–3] All-solid-state sodium batteries with sulfide solid electrolytes are expected to achieve superior

performance because sulfide solid electrolytes exhibit higher ionic conductivities than liquid electrolytes.^[4]

The development of all-solid-state sodium batteries requires high-capacity positive electrode active materials such as sulfur and Na₂S that have high theoretical capacities.^[5–10] However, sulfur and Na₂S are insulating and require the use of large amounts of conductive agents, such as conductive carbons and sulfide electrolytes, leading to a decrease of energy density per a positive electrode. Therefore, it is still necessary to develop positive electrode active materials with high ionic and electronic conductivities and capacities.

Transition-metal sulfides are attractive materials for battery applications due to their high capacity and high conductivity.^[11–14] In particular, iron sulfides and sodium iron sulfides are promising positive electrode active materials^[15–21] due to their high capacity and electronic conductivity that is higher than that of sulfur and due to their abundant constituent elements such as sodium, sulfur, and iron which allow low battery cost. Furthermore, all-solid-state cells using sodium iron sulfides as positive electrode active material can be assembled in the discharged state, expanding the selection of negative electrodes such as carbon^[22] and tin,^[23] and even enabling anode-free cells.^[24] Previous studies have reported on several sodium iron sulfides as positive electrode active materials. For example, Na₆FeS₄ was used in sodium batteries with liquid electrolytes, achieving a high capacity of 440 mAh g⁻¹ at 0.1C rate.^[25] In addition, all-solid-state sodium batteries using Na₂FeS₂ exhibited a high charge–discharge capacity of ≈300 mAh g⁻¹ and operated reversibly over 300 cycles,^[26] indicating that sodium iron sulfides are promising positive electrode active materials for sodium batteries. Scalable synthesis of positive electrode active materials is required for practical application of all-solid-state sodium batteries. Recently, we developed an ambient-pressure process for the synthesis of sodium-containing sulfides such as

Y. Doi, T. Otono, Y. Fujita, R. Kato, M. Torii, K. Motohashi, A. Sakuda, A. Hayashi

Graduate School of Engineering

Department of Applied Chemistry

Osaka Metropolitan University

1-1 Gakuen-cho Naka-ku, Sakai, Osaka 599-8531, Japan

E-mail: saku@omu.ac.jp

J. Ding, S. Mori

Graduate School of Engineering

Department of Materials Science

Osaka Metropolitan University

1-1 Gakuen-cho Naka-ku, Sakai, Osaka 599-8531, Japan

 Supporting information for this article is available on the WWW under <https://doi.org/10.1002/batt.202500551>

 © 2025 The Author(s). *Batteries & Supercaps* published by Wiley-VCH GmbH. This is an open access article under the terms of the Creative Commons Attribution License, which permits use, distribution and reproduction in any medium, provided the original work is properly cited.

Na_3BS_3 ,^[27] $\text{Na}_{2.88}\text{Sb}_{0.88}\text{W}_{0.12}\text{S}_4$,^[27] $\text{Na}_3\text{BS}_3\text{-SiO}_2$,^[28] and $\text{Na}_4\text{SiS}_4\text{-SiO}_2$,^[29] through flux synthesis via sodium polysulfides.

In this study, Na_5FeS_4 was investigated as a positive electrode active material for all-solid-state sodium batteries and synthesized under ambient pressure using sodium polysulfides for the first time. The structure of the obtained Na_5FeS_4 sample was evaluated using X-ray diffraction (XRD), scanning electron microscopy (SEM), Raman spectroscopy, X-ray photoelectron spectroscopy (XPS), and transmission electron microscopy (TEM). The ionic and electronic conductivities of the sample were investigated. Then, Na_5FeS_4 was used as the positive electrode active material for all-solid-state sodium batteries, and charge-discharge tests were performed, demonstrating a high reversible capacity. In addition, the structure and morphology of the positive electrode layer were evaluated before and after the charge-discharge tests to elucidate the origin of the observed favorable characteristics of the all-solid-state sodium batteries.

2. Results and Discussion

The crystal structure of the sample synthesized in this study using the flux method was compared with the structure of Na_5FeS_4 synthesized by heating a pelletized mixture of Na_2S , Fe, and S in a vacuum-sealed quartz ampoule for 2 days that was reported in a previous study.^[30] Figure 1a shows the Rietveld refinement of the XRD pattern of the prepared Na_5FeS_4 . The good match of the fitted pattern confirms that Na_5FeS_4 was successfully synthesized via sodium polysulfides. Table S1, Supporting Information, summarizes the results of the Rietveld refinement, and the crystal

structure of Na_5FeS_4 is shown in Figure 1b. In agreement with the previous reports, the Na_5FeS_4 prepared in this study belongs to the *Pbca* orthorhombic space group, with lattice parameters $a = 11.9638(3)$ Å, $b = 7.09871(18)$ Å, and $c = 21.5755(6)$ Å. The isolated FeS_4 tetrahedra are arranged in the *a-b* plane, and approximately six Na atoms coordinate each S atom (Figure S1, Supporting Information).

The prepared Na_5FeS_4 was observed by SEM as shown in Figure 2a. The SEM image reveals the presence of submicron-scale secondary particles. Figure 2b shows the Na, S, and Fe elemental mappings obtained by energy-dispersive X-ray spectroscopy (EDS) of Na_5FeS_4 . Na, S, and Fe were uniformly distributed throughout the samples, and no impurities were observed.

Raman spectroscopy was conducted to evaluate the local structure of Na_5FeS_4 . This study is the first to report the Raman spectrum of Na_5FeS_4 and therefore, first-principles calculations of the Raman spectra were performed to accurately assign the Raman bands. Figure 3a shows the experimentally obtained Raman spectrum of Na_5FeS_4 and the spectrum calculated based on its crystal structure. In the experimental spectrum, two bands were observed at ≈ 340 and 370 cm $^{-1}$, while the calculated spectrum exhibited a main peak at 336 cm $^{-1}$ and another peak at 369 cm $^{-1}$, in good agreement with the peaks at 340 and 370 cm $^{-1}$ observed experimentally. According to the first-principles calculations, the peak at 336 cm $^{-1}$ originated mainly from the symmetric stretching vibration of the FeS_4 tetrahedral units, suggesting that the band at 340 cm $^{-1}$ in the experimental spectrum is primarily due to this vibration mode. Furthermore, several additional peaks appear near the main peak, suggesting that the vibrational modes of Na_5FeS_4 are complex.

Figure 3b shows the XPS S 2p spectrum of Na_5FeS_4 and the reference spectra of Na_2S and Na_2FeS_2 .^[26] The S 2p spectra typically exhibits doublet peaks corresponding to $\text{S} 2\text{p}_{3/2}$ and $\text{S} 2\text{p}_{1/2}$. Because the $\text{S} 2\text{p}_{3/2}$ peak has a higher intensity than the $\text{S} 2\text{p}_{1/2}$ peak, only the $\text{S} 2\text{p}_{3/2}$ peaks are discussed in this study. The S 2p spectrum of Na_5FeS_4 showed a peak at ≈ 159.6 eV, which is attributed to the FeS_4 units in the Na_5FeS_4 crystal structure. The electronic state of sulfur in Na_5FeS_4 appears to be similar to that of sulfur in Na_2S rather than to that of sulfur in Na_2FeS_2 . Figure S1 and S2, Supporting Information, show the local structure around the sulfur in Na_5FeS_4 and Na_2FeS_2 , respectively. Because sulfur is coordinated by more Na atoms in Na_5FeS_4 than in Na_2FeS_2 , its electronic state exhibits a lower binding energy. The peak at ≈ 161.3 eV is attributed to a small amount of oxidized sulfur species.

Then, the ionic and electronic conductivities of Na_5FeS_4 were investigated. Generally, the ionic and electronic conductivities of composite electrodes consisting of a mixture of a solid electrolyte and electronic conductor are determined by DC polarization measurements using electron- and ion-blocking cells, respectively.^[31,32] Following this approach, both an electron-blocking cell (Figure 4a) and ion-blocking cell (Figure 4b) were assembled, and DC measurements were conducted. Figure 4c and d show the DC curves of the electron-blocking cell and the ion-blocking cell, respectively. While the current was stable in the electron-blocking cell (Figure 4c) during the DC measurement, it gradually decreased for the ion-blocking cell (Figure 4d), possibly due to

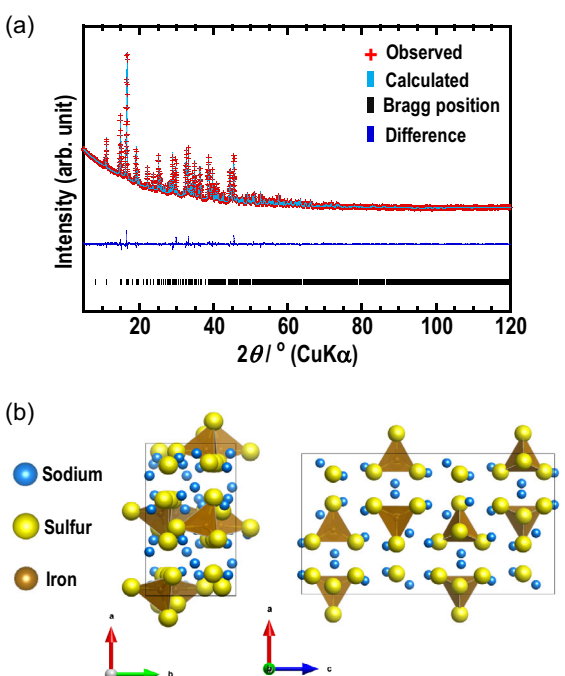


Figure 1. a) Refined XRD pattern and b) crystal structure of Na_5FeS_4 . Blue spheres, yellow spheres, and brown tetrahedra represent Na, S, and FeS_4 , respectively.

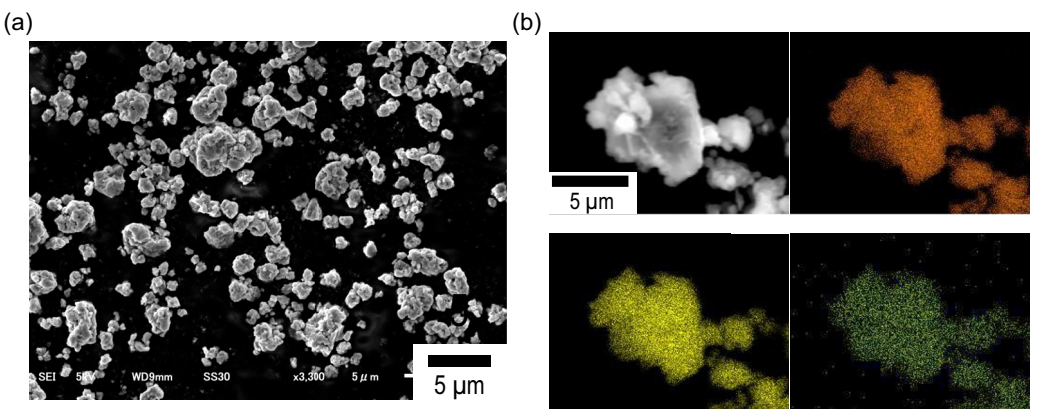


Figure 2. a) SEM image of a wide field of view and b) EDS elemental mappings for Na, S, and Fe of Na_5FeS_4 .

the charge transfer reaction and ion diffusion occurring at the interface between the current collector and Na_5FeS_4 .

The ionic conductivity of Na_5FeS_4 was also investigated by AC impedance spectroscopy. When the ionic conductivity is sufficiently higher than the electronic conductivity, the Nyquist plots obtained by AC impedance measurements for the ion-blocking cells should show typical profiles for ionic conductors, characterized by one semicircle and a spike. Figure 4e shows the Nyquist plots obtained by AC impedance spectroscopy of the ion-blocking cell. A semicircle derived from the resistance originating from ionic conduction is observed in the high-frequency region, and a straight line derived from ion diffusion is observed in the low-frequency region. The resistance originating from the

charge-transfer reaction is much lower than the ionic conduction and diffusion resistances. Figure S3, Supporting Information, shows the Nyquist plots obtained from ion-blocking cells with different thicknesses. It was observed that the semicircle expanded with increasing pellet thickness, confirming that it originated from the ionic conduction resistance. By contrast, the length of the straight line remained constant regardless of the pellet thickness, confirming that it originated from ion diffusion at the interface between the electrode and the current collector. These measurements reveal that the ionic conductivity of Na_5FeS_4 is much higher than its electronic conductivity. The ionic conductivity of Na_5FeS_4 determined by DC polarization measurement using an electron-blocking cell and by AC impedance spectroscopy using an ion-blocking cell showed good agreement, with both methods obtaining values of $\approx 1.0 \times 10^{-6} \text{ S cm}^{-1}$. Owing to the significant contribution of the electrode reaction, the electronic conductivity of Na_5FeS_4 could not be determined using the ion-blocking cell.

To evaluate the charge-discharge characteristics, all-solid-state cells were assembled using Na_5FeS_4 as the positive electrode active material. Figure 5 shows the charge-discharge curves of the cell under a current density of 0.13 mA cm^{-2} at $\approx 25^\circ\text{C}$. The cell exhibited an initial charge capacity of 430 mAh g^{-1} , which is close to the theoretical capacity of 448 mAh g^{-1} for a 5-electron reaction; this is due to the sufficient ionic conductivity of Na_5FeS_4 . The initial discharge capacity was 480 mAh g^{-1} , exceeding the charge capacity, which is explained by the insertion of additional Na^+ from the $\text{Na}-\text{Sn}$ alloy negative electrode into the active material. Starting at the second charge, the charge-discharge capacities remained at $\approx 480 \text{ mAh g}^{-1}$, indicating stable and reversible cycling. To understand the charge-discharge reaction of Na_5FeS_4 , the open-circuit voltage (OCV) during the initial cycling was investigated using an intermittent charge-discharge test. Figure S4a and b, Supporting Information, show the charge-discharge and OCV curves of the all-solid-state cells using Na_5FeS_4 . The initial charge capacity was $\approx 470 \text{ mAh g}^{-1}$, exceeding the theoretical capacity of Na_5FeS_4 (448 mAh g^{-1}). This excess capacity is contributed by the oxidation of the solid electrolyte in the composite positive

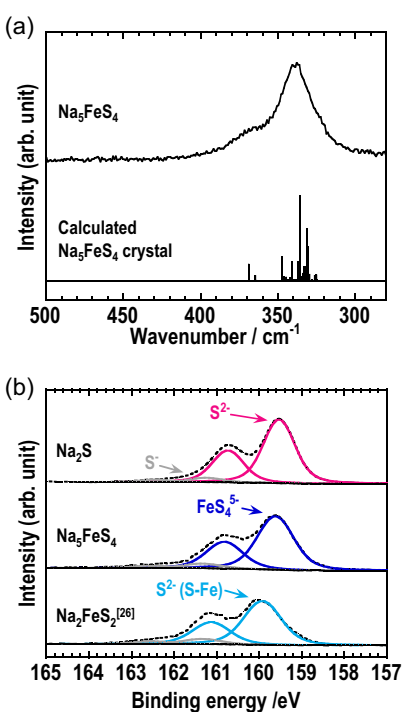


Figure 3. a) Measured and calculated Raman spectra of Na_5FeS_4 . b) XPS S 2p spectrum of Na_5FeS_4 and reference spectra of Na_2S and $\text{Na}_2\text{FeS}_2^{[26]}$.

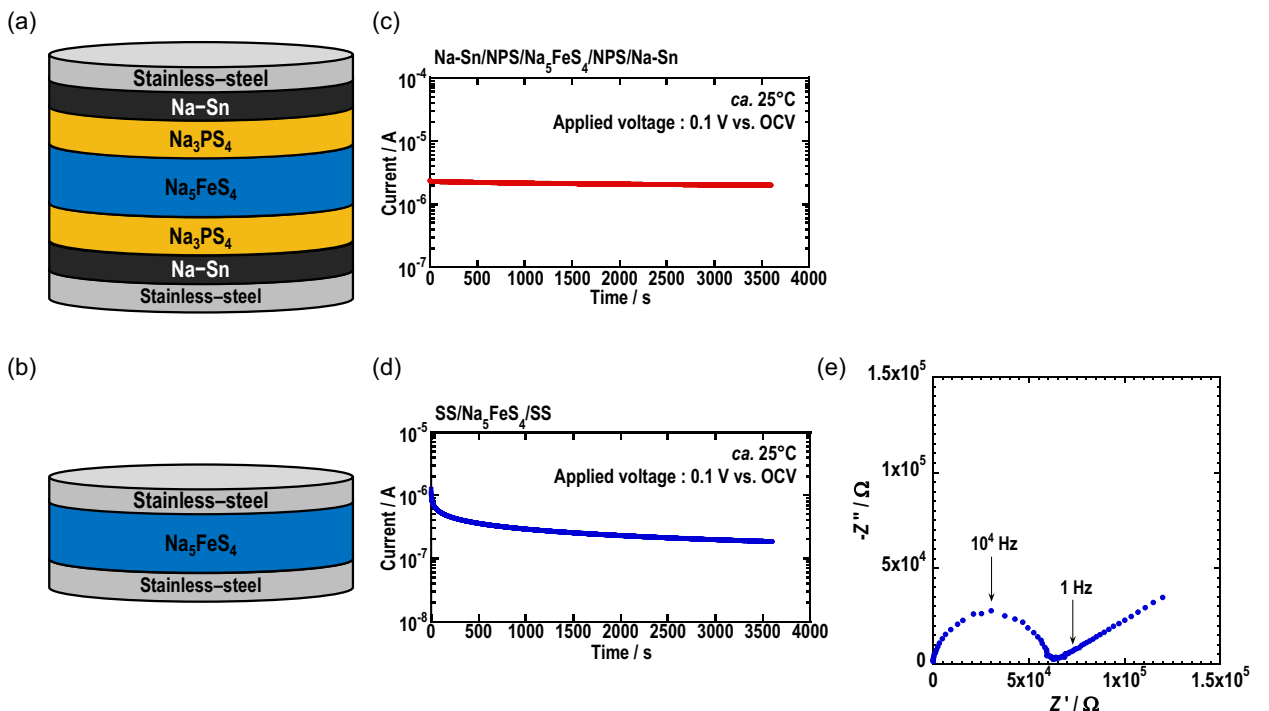


Figure 4. Schematic of the a) electron-blocking cell (Na-Sn/Na₃PS₄/Na₅FeS₄/Na₃PS₄/Na-Sn) and b) ion-blocking cell (stainless-steel/Na₅FeS₄/stainless-steel). c) Time-current diagrams measured by DC polarization measurement of the electron-blocking cell at $\approx 25^{\circ}\text{C}$. d) Time-current diagrams obtained by DC polarization measurements and e) Nyquist plots of the ion-blocking cell at $\approx 25^{\circ}\text{C}$.

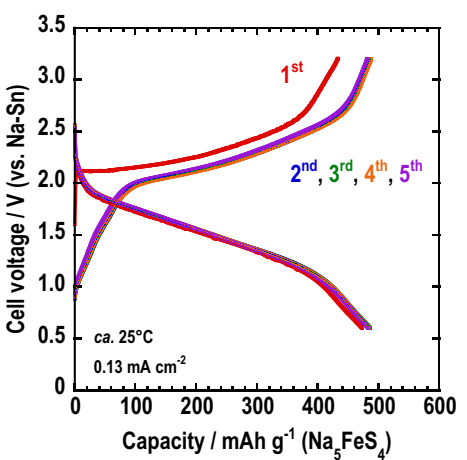


Figure 5. Charge-discharge curves for 5 cycles of all-solid-state cells with Na-Sn/Na₃PS₄/Na₅FeS₄-Na₃PS₄-AB.

electrode. A large overvoltage was observed at the start of charging, which was attributed to the low electronic conductivity of the active material.

To investigate the charge-discharge mechanism of Na₅FeS₄, the structure of the positive electrode before and after charging and discharging was characterized using XRD, TEM, XPS, and SEM. Figure 6a shows the XRD patterns of the positive electrode layers before and after the initial charge-discharge cycles. Before cycling, the diffraction patterns of Na₅FeS₄ (shown in blue) and Na₃PS₄ solid electrolyte (shown in red) were observed. The diffraction peaks of Na₅FeS₄ disappeared during the initial charge,

suggesting the amorphization of the active material. After discharging, no diffraction peaks corresponding to the active material were observed, and only the diffraction pattern of Na₃PS₄ was observed, indicating that the amorphous state of the active material was maintained. Figure S5a, Supporting Information, shows the electron diffraction (ED) pattern of the Na₅FeS₄ before cycling, and Figure S5b, Supporting Information, shows the corresponding dark-field TEM image. The bright contrast area, which was marked by the yellow arrow, is the Na₅FeS₄ crystal. Figure S6a, Supporting Information, shows the bright-field TEM image of the positive electrode layer after the initial discharge. In Figure S6b, the ED pattern of the active material exhibited only halo rings, indicating that, within the resolution of TEM observation, most of the active material was amorphous, which was consistent with the XRD results. Thus, the XRD measurements and TEM observations suggested that the active material was amorphized during the initial charge and retained its amorphous state during the initial discharge. This amorphization is considered to allow the active material to store Na corresponding to more than five electrons.

Figure 6b shows the XPS S 2p spectra of the positive electrode layer before and after the initial charge and discharge. Note that, the cells fabricated in this study, the Na₅FeS₄ active material and Na₃PS₄ solid electrolyte were not sufficiently uniform, leading to variations in the Na₅FeS₄/Na₃PS₄ ratio between measurements. Before cycling, the peaks at 159.6 and 161.1 eV, originating from Na₅FeS₄ and Na₃PS₄, respectively, were observed. After charging, the peak at 159.6 eV derived from Na₅FeS₄ shifted to higher binding energy, indicating that the sulfur in Na₅FeS₄ was oxidized

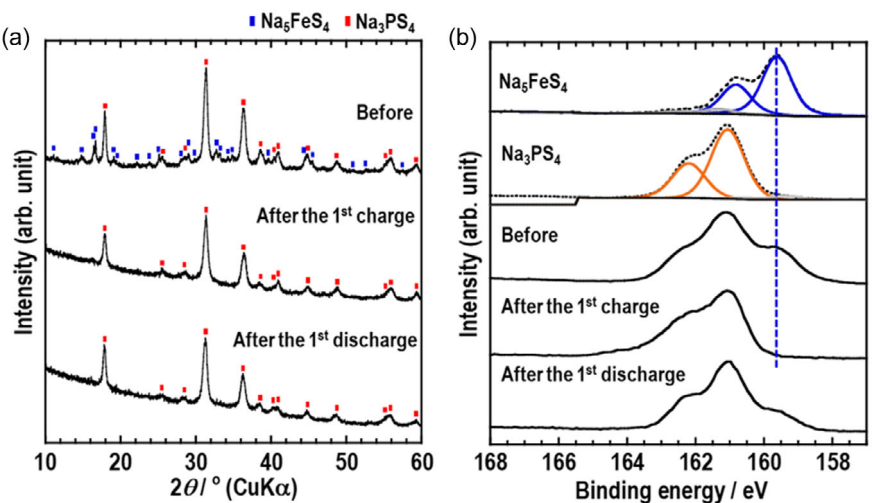


Figure 6. Ex situ a) XRD patterns and b) XPS S 2p spectra of the positive electrode before and after the initial charging and discharging.

during the charging process. After discharging, an electronic state similar to that before charging was observed, suggesting that the electronic state of sulfur in the active material underwent reversible redox reactions, even though a detailed analysis was hindered by the presence of sulfur in the solid electrolyte. It is considered that all sulfur in the active material contributes to the charge-discharge capacity. Figure S7, Supporting Information, shows the XPS P 2p, and Fe 2p spectra of the positive electrode layer before and after the initial charge and discharge. From the XPS P 2p spectra, it was confirmed that the Na_3PS_4 electrolyte slightly oxidized during charging but did not significantly change. The Fe 2p spectra did not change significantly during the initial cycle.

Figure 7 shows cross-sectional SEM images and EDS mappings of the positive electrode layer before and after the initial cycle. Before charging and discharging, Na and S were distributed throughout the positive electrode layer. After initial charging, Na was barely detected in the active material region where Fe was located, indicating that Na was almost completely extracted from the Na_5FeS_4 positive electrode active material during the initial charge. After discharging, Na was observed in the active material region, indicating that Na was inserted into the active material during the initial discharge. Table S2, Supporting Information, shows the EDS analysis results for the active material region before and after charging and discharging. The Na/Fe ratio before charging was 5.0, which was consistent with the composition of Na_5FeS_4 . The Na/Fe ratio was ≈ 0.2 after charging and 5.7 after discharging, which was quite close to the ratio for the composition of the active material estimated from the charge and discharge capacities. The extraction and insertion of Na in relatively large active material particles of several micrometers suggests that the active material has a high ionic diffusivity, consistent with the results of the conductivity measurements described above. The SEM image obtained before cycling indicates that the particles are in good contact with each other, and the active material and solid electrolyte form a dense interface. Since the sulfur acting as the positive electrode active material undergoes significant volume changes, it is difficult to

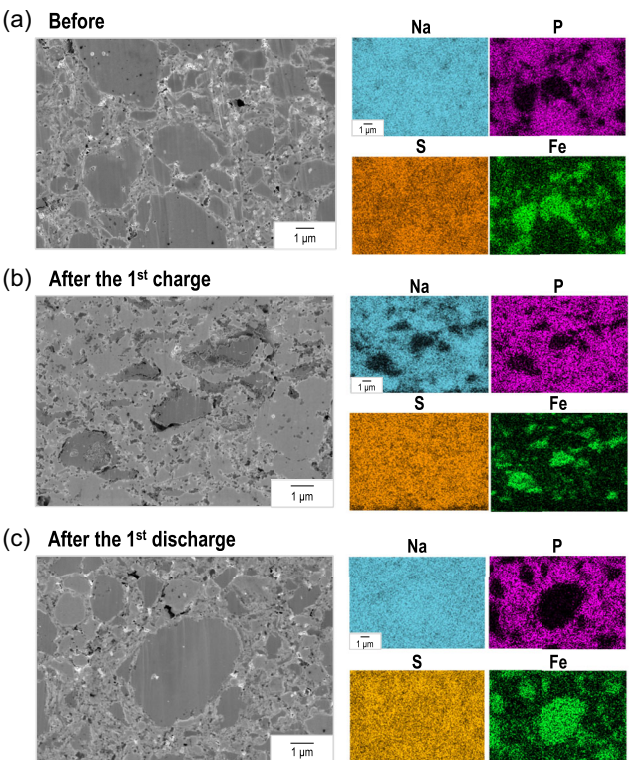


Figure 7. Cross-sectional SEM images and EDS elemental mappings for Na, P, S, and Fe in composite electrode of the all-solid-state cell using Na_5FeS_4 , a) before, b) after the initial charging, and c) after the initial discharging.

maintain an active material/solid electrolyte interface within the positive electrode composite.^[33] By contrast, the composite positive electrode using Na_5FeS_4 maintained contact at the active material/solid electrolyte interface, and the ion conduction pathways to the active material were retained, allowing the subsequent charge and discharge to proceed. Thus, SEM-EDS observations showed that complete Na extraction and insertion, and maintenance of the interface led to high cell performance.

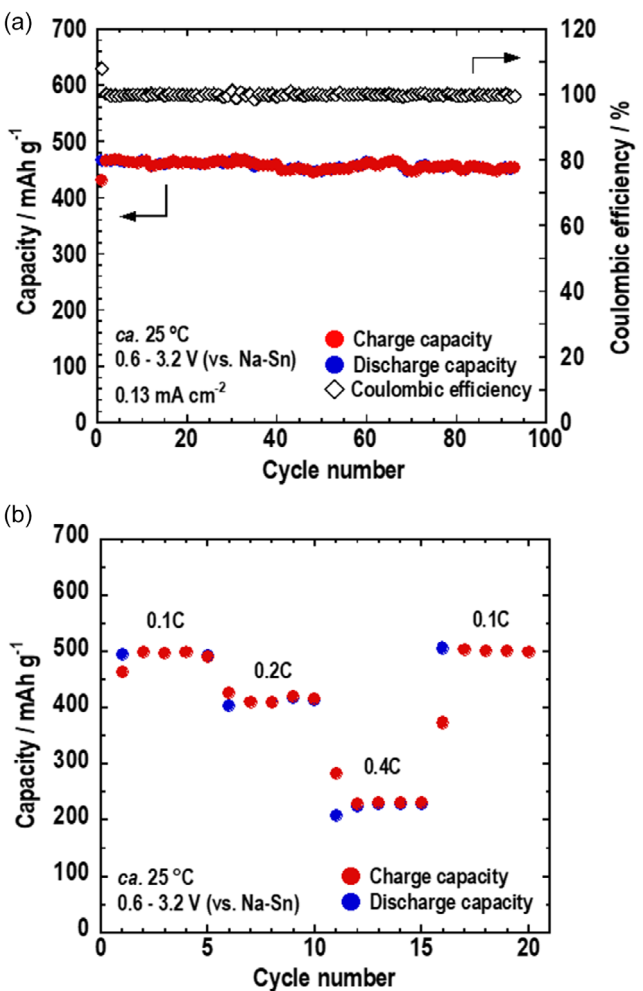


Figure 8. a) Cycle and b) rate performance of all-solid-state cells with Na-Sn/Na₃PS₄/Na₅FeS₄-Na₃PS₄-AB at ≈ 25 °C.

Figure 8a,b show the cycle and rate performance of the all-solid-state cell using Na₅FeS₄. In the cycle test, the cell exhibited a high charge-discharge capacity of 460–480 mAh g⁻¹ over 90 cycles. In the rate test, the cell exhibited charge-discharge capacities of ≈ 400 mAh g⁻¹ and 230 mAh g⁻¹ at the rates of 0.2C and 0.4C, respectively (1C = 448 mA g⁻¹). Owing to the sufficient ionic conductivity of Na₅FeS₄ and the maintenance of the active material/sulfide solid electrolyte interface, high cell performance was achieved.

3. Conclusion

Na₅FeS₄ was synthesized at ambient pressure using sodium poly-sulfides and the local structure of Na₅FeS₄ was studied for the first time. The ionic and electronic conductivities of Na₅FeS₄ were carefully evaluated, revealing that the ionic conductivity was higher than the electronic conductivity, with a value of $\approx 1.0 \times 10^{-6}$ S cm⁻¹. All-solid-state cells were fabricated using Na₅FeS₄ as the positive electrode active material, and the cells exhibited high charge-discharge capacities of 480 mAh g⁻¹ that are close

to the theoretical capacity. The high capacity was attributed to the sufficiently high ionic conductivity of Na₅FeS₄ and the maintenance of the active material/solid electrolyte interface in the positive electrode composite. Structural analysis carried out before and after charging and discharging revealed that the active material was mainly amorphized during the initial charging process and retained its amorphous state in subsequent cycling. The amorphous phase enables reversible charge-discharge cycling and allows the maintenance of a high capacity. This work demonstrates a new positive electrode active material that enhances the performance of all-solid-state sodium batteries with high energy density, high safety, and low cost for large-scale energy storage.

4. Experimental Section

Material Synthesis

All procedures were conducted in dry Ar atmosphere. Na₅FeS₄ was prepared via heat treatment and subsequent quenching. Na₂S (Nagao Co. Ltd., 99.1%), Fe (Kojundo Chemical, 99.9%), and S (Kojundo Chemical, 99.99%) used as the starting materials were mixed in an agate mortar. The mixture was placed in a carbon crucible and heated in an electric furnace at 750 °C for 10 h under ambient pressure to obtain Na₅FeS₄ melts which were then subjected to iron press quenching. The Na₃PS₄ solid electrolyte was prepared using a mechanochemical process followed by heat treatment.^[34] The starting materials of 75 mol% Na₂S (Nagao Co. Ltd.) and 25 mol% P₂S₅ (Sigma-Aldrich Co. Ltd., 99.9%) were hand-ground, and the mixture was then placed in a zirconia (ZrO₂) vessel (internal volume of 250 mL) with ZrO₂ balls (450 g, 4 mm in diameter). Mechanochemical reaction was performed for 1.5 h at a fixed rotational speed of the base disk of 210 rpm. The prepared sample was then heated at 225 °C for 2 h in an electric furnace to prepare the glass-ceramics. The composite positive electrode was prepared by mixing Na₅FeS₄, Na₃PS₄, and acetylene black in a mortar in a weight ratio of 40:60:6. The negative electrode were composed of Na₁₅Sn₄ and Ketjen black and were prepared by mechanochemical alloying.^[35]

Material Characterization

All procedures were conducted in dry Ar atmosphere. XRD measurements were performed using a diffractometer (SmartLab, Rigaku) with Cu K α radiation ($\lambda = 1.54059 \times 10^{-10}$ m). The powder sample was placed in an airtight sample holder with a Kapton film window, and the pellet sample was placed in an airtight sample holder with a Be window for measurement. The crystal structure was refined using the PDXL2 computer program (Rigaku), and the crystal models were visualized using the VESTA software.^[36] Rietveld refinement was performed for the XRD data collected in the 2 θ range of 10°–120° at a scan rate of 2° min⁻¹. Raman analysis was performed using a Raman spectrophotometer (LabRAM HR-800; Horiba) with a 532 nm solid-state laser. The powder samples were placed on a Raman sample stage and hermetically sealed with a cover glass in dry Ar atmosphere. The electronic states of S in the obtained samples were analyzed by XPS (K-Alpha, Thermo Fisher Scientific) with a monochromatic Al K α light source (1486.6 eV). The powder or pellet samples were placed in a vessel and hermetically sealed with a cover glass in dry Ar atmosphere. The data from the surface was analyzed after calibration to 84.0 eV for Au 4d. SEM-EDS observations of the powdered Na₅FeS₄ were performed using a field-emission scanning

electron microscope (JSM-6610A, JEOL Ltd.) equipped with an EDS system (EX94320S3L2Q, JEOL Ltd.). The cross-sections of the positive electrodes were prepared using an Ar-ion milling system (E-3500; Hitachi High-Technologies Corp.), and cross-sectional images were acquired using field-emission SEM (SU8220, Hitachi High-Technologies Corp.). The Raman spectrum of the Na_5FeS_4 crystal was calculated using density functional theory (DFT).^[37,38] All DFT calculations were performed with the Vienna ab initio simulation package (VASP)^[39,40] using the Perdew–Burke–Ernzerhof (PBE) formulation of the generalized gradient approximation (GGA) for the exchange-correlation functional.^[41,42] The projected augmented wave (PAW) method^[43,44] was used to describe the pseudopotentials of the inner shell electrons. A cut-off energy of 500 eV was applied for the plane wave basis set, and the electronic energy convergence criterion was set at 10^{-5} eV. The k-point sampling of the irreducible Brillouin zone was carried out using the Monkhorst–Pack method.^[45] The lattice constants and ionic positions of the ordinary crystal structures were fully relaxed, ensuring that the final forces on all relaxed atoms were less than 0.01 eV/ \AA . These calculations incorporate the DFT-D3 method with the Becke-Johnson damping function.^[46] Spin polarization was not considered in the DFT calculations. The CIF file of the Na_5FeS_4 crystal was obtained from the ICSD^[47] crystal structure database. After structural optimization, the phonon frequencies were calculated and the peak intensities of the Raman spectrum were computed using the "raman_sc" program.^[48,49] The TEM observations were conducted using a JEM-2100Plus (JEOL Co., Ltd.) instrument at an accelerating voltage of 200 kV. TEM observation samples were prepared using a focused ion beam (FIB) apparatus (JIB-4700F, JEOL Co., Ltd.). During TEM observations, a vacuum transfer TEM holder (MeI-Build) was used to avoid exposing the samples to air. A complementary metal-oxide-semiconductor camera (OneView, Gatan Inc.) was used to record.

Assembly of All-Solid-State Cells and Charge–Discharge Tests

All-solid-state cells with $\text{Na}-\text{Sn}/\text{Na}_3\text{PS}_4/\text{Na}_5\text{FeS}_4-\text{Na}_3\text{PS}_4-\text{AB}$ were assembled for galvanostatic charge–discharge tests. Na_3PS_4 solid electrolyte (80 mg) was placed in a polycarbonate tube (diameter = 10 mm) and pressed moderately. A composite positive electrode (≈ 6.0 mg) was placed on the surface of the separator layer and pressed at 180 MPa for 1 min. The negative electrode was placed on the opposite side of the separator layer and pressed at 360 MPa for 5 min. Stainless steel rods were used as current correctors. The assembled all-solid-state cells were strained by flames, and the applied pressure exceeded 50 MPa. The charge–discharge tests were conducted at 25 °C in the voltage range of 0.6–3.2 V under Ar atmosphere. The cell performance was evaluated using a potentiostat/galvanostat device (BCS-800, Biologic). The intermittent charge–discharge test was conducted at 0.13 mA cm⁻² with a relaxation time of 5 h. The cycle and rate tests were conducted at 25 °C in the voltage range of 0.6–3.2 V. The rate was changed to 0.1C, 0.2C, 0.4C, and back to 0.1C, with charge–discharge measurements performed for five cycles at each rate.

Electrochemical Characterization

Ion-blocking cells (Stainless steel/ Na_5FeS_4 /Stainless steel) and electron-blocking cells ($\text{Na}_{15}\text{Sn}_4/\text{Na}_3\text{PS}_4/\text{Na}_5\text{FeS}_4/\text{Na}_3\text{PS}_4/\text{Na}_{15}\text{Sn}_4$) were fabricated. The DC polarization measurements were conducted at 25 °C by applying a voltage of 0.1 V for 1 h. The AC impedance measurements were conducted at 25 °C in the frequency range of 0.01 Hz to 1 MHz. AC impedance measurements were performed using ion-blocking cells with the Na_5FeS_4 layer thicknesses of 180, 410, and 560 μm .

Acknowledgements

This research was partially supported by JSPS KAKENHI grant numbers JP21H04701, JP23H02071, and Transformative Research Areas (A) 'Supra-ceramics' (JP23H04633 and JP25H01681).

Conflict of Interest

The authors declare no conflict of interest.

Author Contributions

Atsushi Sakuda conceived the study. **Yuta Doi** and **Tomoya Otono** conducted synthesis and structural evaluations. **Raku Kato** and **Masato Torii** performed the Raman calculations. **Jiong Ding** and **Shigeo Mori** conducted TEM observations. **Yuta Doi** and **Yushi Fujita** wrote the manuscript. **Atsushi Sakuda**, **Kota Motohashi**, and **Akitoshi Hayashi** supervised the study. All authors discussed the results, reviewed the manuscript, and approved the final version.

Data Availability Statement

The data that support the findings of this study are available from the corresponding author upon reasonable request.

Keywords: active materials • all-solid-state battery • positive electrodes • sodium battery • sodium iron sulfide

- [1] B. L. Ellis, L. F. Nazar, *Curr. Opin. Solid State Mater. Sci.* **2012**, *16*, 168.
- [2] H. Pan, Y.-S. Hu, L. Chen, *Energy Environ. Sci.* **2013**, *6*, 2338.
- [3] N. Yabuuchi, K. Kubota, M. Dahbi, S. Komaba, *Chem. Rev.* **2014**, *114*, 11636.
- [4] A. Hayashi, N. Masuzawa, S. Yubuchi, F. Tsuji, C. Hotchama, A. Sakuda, M. Tatsumisago, *Nat. Commun.* **2019**, *10*, 5266.
- [5] J. Ma, M. Wang, H. Zhang, Z. Shang, L. Fu, W. Zhang, B. Song, K. Lu, *Adv. Funct. Mater.* **2023**, *33*, 2214430.
- [6] L. Zhao, Y. Tao, Y. Zhang, Y. Lei, W.-H. Lai, S. Chou, H.-K. Liu, S.-X. Dou, Y.-X. Wang, *Adv. Mater.* **2024**, *36*, e2402337.
- [7] N. Tanibata, M. Deguchi, A. Hayashi, M. Tatsumisago, *Chem. Mater.* **2017**, *29*, 5232.
- [8] T. Ando, S. Yubuchi, A. Sakuda, A. Hayashi, M. Tatsumisago, *Electrochem. Tokyo*, **2019**, *87*, 289.
- [9] T. Ando, A. Sakuda, M. Tatsumisago, A. Hayashi, *Electrochem. Commun.* **2020**, *116*, 106741.
- [10] Y. Fujita, A. Nasu, A. Sakuda, M. Tatsumisago, A. Hayashi, *J. Power Sources* **2022**, *532*, 231313.
- [11] G. Shirota, A. Nasu, M. Deguchi, A. Sakuda, M. Tatsumisago, A. Hayashi, *J. Power Sources Adv.* **2021**, *10*, 100061.
- [12] G. Shirota, A. Nasu, A. Sakuda, M. Deguchi, K. Motohashi, M. Tatsumisago, A. Hayashi, *Electrochem. Tokyo* **2022**, *90*, 037011.
- [13] G. Shirota, A. Nasu, M. Deguchi, A. Sakuda, M. Tatsumisago, A. Hayashi, *Solid State Ion.* **2022**, *376*, 115848.
- [14] G. Shirota, A. Nasu, M. Deguchi, A. Sakuda, M. Tatsumisago, A. Hayashi, *J. Ceram. Soc. Jpn* **2022**, *130*, 308.
- [15] T. B. Kim, J. W. Choi, H. S. Ryu, G. B. Cho, K. W. Kim, J. H. Ahn, K. K. Cho, H. J. Ahn, *J. Power Sources* **2007**, *174*, 1275.
- [16] T. B. Kim, W. H. Jung, H. S. Ryu, K. W. Kim, J. H. Ahn, K. K. Cho, G. B. Cho, T. H. Nam, I. S. Ahn, H. J. Ahn, *J. Alloys Compd.* **2008**, *449*, 304.
- [17] A. Kitajou, J. Yamaguchi, S. Hara, S. Okada, *J. Power Sources* **2014**, *247*, 391.

- [18] A. Douglas, R. Carter, L. Oakes, K. Share, A. P. Cohn, C. L. Pint, *ACS Nano* **2015**, *9*, 11156.
- [19] Y. Zhu, L. Suo, T. Gao, X. Fan, F. Han, C. Wang, *Electrochem. Commun.* **2015**, *54*, 18.
- [20] T. Takeuchi, H. Kageyama, N. Taguchi, K. Nakanishi, T. Kawaguchi, K. Ohara, K. Fukuda, A. Sakuda, T. Ohta, T. Fukunaga, H. Sakaebi, H. Kobayashi, E. Matsubara, *Solid State Ion.* **2018**, *320*, 387.
- [21] K. Shimoda, M. Murakami, T. Takeuchi, T. Matsunaga, Y. Ukyo, H. Sakaebi, H. Kobayashi, E. Matsubara, *J. Power Sources* **2018**, *398*, 67.
- [22] H. Hou, X. Qiu, W. Wei, Y. Zhang, X. Ji, *Adv. Energy Mater.* **2017**, *7*, 1602898.
- [23] Y. Xu, Y. Zhu, Y. Liu, C. Wang, *Adv. Energy Mater.* **2013**, *3*, 128.
- [24] G. Deysher, J. A. S. Oh, Y.-T. Chen, B. Sayahpour, S.-Y. Ham, D. Cheng, P. Ridley, A. Cronk, S. W.-H. Lin, K. Qian, L. H. B. Nguyen, J. Jang, Y. S. Meng, *Nat. Energy* **2024**, *9*, 1161.
- [25] J. He, A. Bhargav, J. Okasinski, A. Manthiram, *Adv. Mater.* **2024**, *36*, e2403521.
- [26] A. Nasu, A. Sakuda, T. Kimura, M. Deguchi, A. Tsuchimoto, M. Okubo, A. Yamada, M. Tatsumisago, A. Hayashi, *Small* **2022**, *18*, e2203383.
- [27] A. Nasu, T. Otono, T. Takayanagi, M. Deguchi, A. Sakuda, M. Tatsumisago, A. Hayashi, *Energy Storage Mater.* **2024**, *67*, 103307.
- [28] T. Otono, A. Nasu, T. Asakura, H. Kowada, K. Motohashi, M. Tatsumisago, A. Sakuda, A. Hayashi, *Inorg. Chem.* **2024**, *63*, 4589.
- [29] T. Otono, A. Nasu, T. Asakura, H. Kowada, K. Motohashi, A. Sakuda, M. Tatsumisago, A. Hayashi, *Adv. Sustain. Syst.* **2024**, *8*, 2400130.
- [30] K. O. Klepp, W. Bronger, Z. Anorg. Allg. Chem. **1986**, *532*, 23.
- [31] T. Asano, S. Yubuchi, A. Sakuda, A. Hayashi, M. Tatsumisago, *J. Electrochem. Soc.* **2017**, *164*, A3960.
- [32] G. F. Dewald, S. Ohno, J. G. C. Hering, J. Janek, W. G. Zeier, *Batter. Supercaps* **2021**, *4*, 183.
- [33] X. Hong, J. Mei, L. Wen, Y. Tong, A. J. Vasileff, L. Wang, J. Liang, Z. Sun, S. X. Dou, *Adv. Mater.* **2019**, *31*, 1802822.
- [34] A. Hayashi, K. Noi, A. Sakuda, M. Tatsumisago, *Nat. Commun.* **2012**, *3*, 856.
- [35] N. Tanibata, A. Hayashi, M. Tatsumisago, *J. Electrochem. Soc.* **2015**, *162*, A793.
- [36] K. Momma, F. Izumi, *J. Appl. Crystallogr.* **2011**, *44*, 1272.
- [37] P. Hohenberg, W. Kohn, *Phys. Rev.* **1964**, *136*, B864.
- [38] W. Kohn, L. J. Sham, *Phys. Rev.* **1965**, *140*, A1133.
- [39] G. Kresse, J. Furthmüller, *Phys. Rev. B Condens. Matter* **1996**, *54*, 11169.
- [40] G. Kresse, J. Furthmüller, *Comput. Mater. Sci.* **1996**, *6*, 15.
- [41] J. P. Perdew, K. Burke, M. Ernzerhof, *Phys. Rev. Lett.* **1996**, *77*, 3865.
- [42] J. P. Perdew, K. Burke, M. Ernzerhof, *Phys. Rev. Lett.* **1997**, *78*, 1396.
- [43] P. E. Blöchl, *Phys. Rev. B Condens. Matter* **1994**, *50*, 17953.
- [44] G. Kresse, D. Joubert, *Phys. Rev. B Condens. Matter* **1999**, *59*, 1758.
- [45] H. J. Monkhorst, J. D. Pack, *Phys. Rev. B* **1976**, *13*, 5188.
- [46] S. Grimme, S. Ehrlich, L. Goerigk, *J. Comput. Chem.* **2011**, *32*, 1456.
- [47] D. Zagorac, H. Müller, S. Ruehl, J. Zagorac, S. Rehme, *J. Appl. Crystallogr.* **2019**, *52*, 918.
- [48] Github, *VASP: Python Program to Evaluate Off-Resonance Raman Activity Using VASP Code as the Backend*.
- [49] D. Porezag, M. R. Pederson, *Phys. Rev. B Condens. Matter* **1996**, *54*, 7830.

Manuscript received: July 19, 2025

Revised manuscript received: October 3, 2025

Version of record online:
